


Cr₂S₃ a bipolar semiconducting fully compensated ferrimagnetYisehak Gebredingle,^{1,*} Minwoong Joe,^{2,*†} and Changgu Lee^{1,2,‡}¹*SKKU Advanced Institute of Nanotechnology (SAINT), Sungkyunkwan University, Suwon 16419, South Korea*²*School of Mechanical Engineering, Sungkyunkwan University, Suwon 16419, South Korea* (Received 26 November 2021; revised 28 March 2022; accepted 22 April 2022; published 10 May 2022)

The promises of spintronics have longed for the realization of fully compensated states and full spin polarization. Half-metallic/half-semiconducting (HM/HS) and fully compensated materials are suggested as candidates. We use density functional theory to report that the experimentally realized rhombohedral Cr₂S₃ is a promising candidate as a bipolar magnetic semiconducting (BMS)/HS fully compensated ferrimagnetic (FCFiM) material. Our calculations demonstrate that the uniquely layered structure of Cr₂S₃ produces different interlayer and intralayer *d-p-d* hybridization schemes between Cr atoms. Strong interlayer and weak intralayer antiferromagnetic coupling between different Cr sites make the overall magnetic state a fully compensated structure. The origin of BMS/HS and fully compensated state has been explained by a structural analysis, where magnetic exchange interaction between Cr sites is dependent on bond distance and bond angle of each Cr-centered octahedron. Furthermore, by applying strains perpendicular to the basal plane, distortion of Cr octahedron sites and Cr–Cr distance is altered, resulting in the phase transition of the material both electronically and magnetically from BMS-FCFiM to HS-FCFiM to ferrimagnetic (FiM). These studies enable us to rediscover Cr₂S₃ as a novel class of BMS materials.

DOI: [10.1103/PhysRevMaterials.6.054405](https://doi.org/10.1103/PhysRevMaterials.6.054405)**I. INTRODUCTION**

Since the enlightenment of the possibility of half-metallic fully compensated ferrimagnetic (HM-FCFiM) material, it has been pursued as next-generation spintronic material due to its ability of fully spin-polarized current without exhibiting macroscopic magnetization [1–4]. How spin-polarized states can be accommodated in a fully compensated state was explained by van Leuken and de Groot [1]. (Originally, they used the term antiferromagnetic (AFM) state rather than FCFiM, but FCFiM is an accurate description based on the basic work of Néel. Thus, henceforth, unless mentioned, FCFiM is used throughout our work.) A widely adopted route to reach the HM-FCFiM state is doping that can cause compensation of extra magnetic moment while gap opening for minority spin channel only [1,3,5–9]. The bandgap engineering strategy through doping sets two compensating spin sources in a different sublattice. The associated spin asymmetry and anisotropy in energy dispersion could result in a spin-polarized edge state closed to the Fermi level. This approach can work for a material called half-semiconducting fully compensated (HS-FCFiM) material, for which the material is semiconducting with different bandgaps for each spin channel or a spin-polarized half-semiconducting state with the spins in the valence and conduction bands being oppositely polarized, and yet with net-zero magnetization [8–10].

Heusler compounds have been exploited as a promising candidate due to the presence of one or more sublattices

[11]. Half-metallic property has been associated with the Heusler compounds with L2₁ or C1_b order [12,13]. Recently, the Mn₂Ru_{0.5}Ga compound has been alleged to be an HM-FCFiM [14]. The authors started with Cubic Mn₂Ga films with a half-Heusler C1_b structure and added Ru with a proper ratio to show evidence of half-metallicity. Moreover, pnictides and chalcogenides with hexagonal NiAs-type structures have also been predicted as HM-FCFiM material. Among these hexagonal NiAs-type structure candidates, Sembooshi *et al.* synthesized (Cr₂₃Fe₂₃)S₅₄ and demonstrated its half-metallic character experimentally [15]. Besides, intrinsic ferromagnetism in monolayers observed in two-dimensional (2D) materials seemed promising in realizing novel materials for spintronics [16–19]. However, there have been no experimental reports of HM-FCFiM or HS-FCFiM in 2D materials. One could understand this as HS-FCFiM state require a complex crystal structure such as having two different sublattices to interact magnetically. Many of the theoretically reported HM-FCFiM or HS-FCFiM materials are alloys with complex structures, which are difficult to synthesize or epitaxially grow the proposed candidate materials.

Meanwhile, bipolar magnetic semiconducting (BMS) material can also generate a spin-polarized current like HM/HS material [20]. Moreover, gate voltage can control the carrier's spin direction [20–23]. Such unique characteristic of BMS material is attributed to the band structure where the valence band maximum (VBM) spin channel and conduction band minimum (CBM) spin channel are opposite. Compared with HM/HS material, where only one spin channel is available, BMS material can use both spin channels by applying a gate voltage without an external magnetic field. Thus, BMS material is also suitable for next-generation spintronic devices.

*These authors contributed equally to this work.

†Corresponding authors: mjoe122@skku.edu

‡Corresponding authors: peterlee@skku.edu

Cr_2S_3 is considered as a thermoelectric material with low thermal conductivity [24]. Furthermore, along with recent advances for air-stable 2D magnetic materials, several reports of the synthesis and semiconducting property of Cr_2S_3 have appeared in the literature. Being regarded as a quasi-2D material, Cr_2S_3 has been grown down to one unit-cell-thick and characterized as a ferrimagnetic semiconductor [25]. Thickness-dependent conduction-type transition from p -type to n -type with increasing thickness has evidenced an interesting layered feature of Cr_2S_3 [26]. Moreover, its room temperature photodetection revealed a small-gap semiconducting nature [27].

However, despite the experimental investigations, the comprehensive information on the electronic and magnetic properties of the material is far from being complete, although there are previous studies based on density functional theory (DFT) calculation. Some have used ferromagnetic (FM) spin ordering of Cr_2S_3 to calculate the electronic band structure [28,29]. In contrast, an early experimental investigation has probed AFM order as the ground state, although a ferrilike property at finite temperature is probed with magnetic hysteresis measurement [30].

In this work, we have conducted a DFT study to elucidate the ground state of the rhombohedral Cr_2S_3 its electronic and magnetic properties. The careful observation of structure-property relation explains the unpredicted BMS/HS-FCFiM property exposed in the electronic band structure while straining perpendicular to the basal plane. Under strain, distortion of Cr octahedron sites and Cr–Cr distance is altered, resulting in the phase transition of the material both electronically and magnetically from BMS-FCFiM to HS-FCFiM to FiM state.

II. CALCULATIONAL METHODS

All the spin-polarized first-principle calculations were performed by the commercially available Vienna Ab initio Simulation Package (VASP) [31]. The generalized gradient approximation parametrized by Perdew-Burke-Ernzerhof (PBE) with the Hubbard U method is implemented to describe the exchange-correlation function [32,33]. We employ the PBE version of the projector augmented-wave to treat valence electrons with plane-wave basis set cutoff energy of 500 eV. The relaxed cell structure is guaranteed with force on each atom as low as 0.01 eV/Å after relaxation. The total energy is allowed to converge below 10^{-7} eV. The Brillouin zone is sampled by a Monkhorst mesh of $3 \times 3 \times 2$ k points [34]. Collinear spin orientation has been used for all ground state and electronic band calculations to reveal the BMS/HS property of the system. The magnetic anisotropy energy (MAE) is defined as the difference between energies corresponding to the magnetization in the in-plane and out-of-plane directions ($\Delta E = E_{\perp} - E_{\parallel}$). Therefore, a positive (negative) value of MAE indicates an in-plane (out-of-plane) easy axis. After self-consistent ground states were achieved, noncollinear and non-self-consistent calculations were performed to evaluate the total energies. In all MAE calculations, spin-orbit interaction was taken into consideration. The initial structure in the calculation was generated from Refs. [30,35].

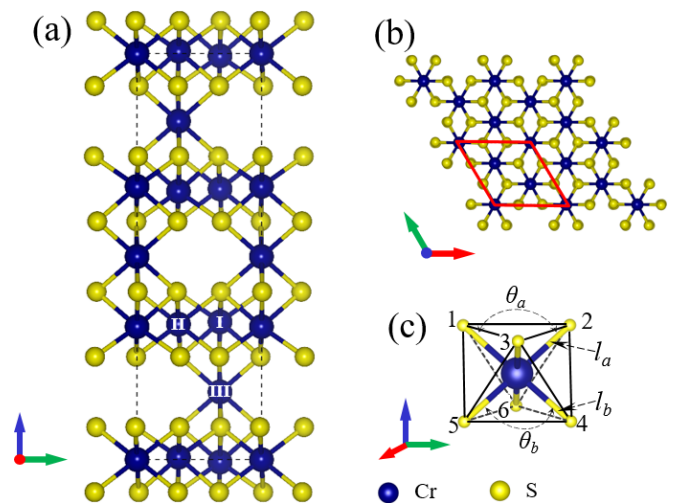


FIG. 1. Schematic representation of the crystal structure. (a) side and (b) top views of a unit cell Cr_2S_3 . Three different Cr sites are indicated in (a) as I, II, and III. (c) Octahedral arrangement of CrS₆. S-atoms in (c) are numbered based on their orientation relative to Cr-atom on the c -axis. (i.e., 1–3 above, 4–6 below Cr atom) Cr–S bond distances and S–Cr–S bond angles are indicated by l_a , l_b , θ_a , and θ_b .

III. RESULTS AND DISCUSSIONS

The crystal structure of Cr_2S_3 is a typical deficient NiAs-type rhombohedral structure in which alternating fully occupied “CrS” layers with Cr-deficient “ $\text{Cr}_{1/3}\text{S}$ ” layers are stacked along the c axis. X-ray powder diffraction measurement at cryogenic temperatures has given rhombohedral structure with lattice dimensions of $a = 5.94$ Å and $c = 16.73$ Å (space group: R-3, 148) [30,35]. The crystal structure has three unique Cr sites, which interact magnetically to give an antiferromagnetic phase with a weak magnetization below Néel temperature of $T_N = 120$ K [30,35]. Figure 1(a) depicts a type of “layered” material, in which “CrS” layers and “ $\text{Cr}_{1/3}\text{S}$ ” layers are clearly shown. Different Cr sites are labeled as I, II, III on Cr atoms. Cr atoms occupy octahedral voids, created by the hexagonal ordering of S atoms shown in Figs. 1(b) and 1(c). Neutron diffraction investigation has revealed that both interlayer interaction between Cr(I) and Cr(III) and intralayer interaction between Cr(I) and Cr(II) have an antiferromagnetic coupling [30,35]. Weak magnetization shown in experimental results was explained by differences in occupancy of the three nonequivalent Cr sites, temperature-dependent magnetic moments, or spin canting [26,35–37].

We first investigate the ground-state magnetic ordering of Cr_2S_3 . An energy comparison was made among four different configurations to determine the magnetic ground state: ferromagnetic, ferrimagnetic (FiM-I and FiM-II), fully compensated ferrimagnetic (FCFiM) as well as nonmagnetic (NM) system. A neutron diffraction investigation at cryogenic temperatures has confirmed that crystallographic and magnetic unit cells are of the same size [35]. Therefore, in all our ground state investigations, we used a rhombohedral structure as a magnetic unit cell. Schematic representations of different configurations of spin ordering are shown in

TABLE I. Lattice parameters a and c in Å; Energy difference ΔE (meV per formula unit); net magnetic moment M and atomic magnetic moment m (in units of μ_B) for different sites. The energy difference is computed using the energy of FCFiM structure as a reference. The arrows refer to spin states of Cr atoms in sites I, II, and III with their respective orders [Fig. 1(a)].

Magnetic Ordering	a	c	ΔE	M	m		
					Cr(I)	Cr(II)	Cr(III)
FM ($\uparrow\uparrow\uparrow$)	6.05	16.97	19.40	36	3.08	3.06	3.15
FiM-I ($\uparrow\downarrow\uparrow$)	5.96	17.15	6.76	18	2.97	-2.84	3.07
FiM-II ($\uparrow\uparrow\downarrow$)	6.06	16.51	41.68	18	2.99	2.99	-2.78
FCFiM ($\uparrow\downarrow\downarrow$)	5.97	16.86	0	0	2.88	-2.89	-2.88
NM	5.57	16.59	2176.7			N/A	
FCFiM [25]	5.94	16.73	N/A	0		N/A	
FCFiM [42]	5.93	16.68	N/A	0		N/A	

Fig. S1 within the Supplemental Material (SM) [38]. The FCFiM magnetic structure can be represented as P-1 (2.4) ($a, -1/3a+1/3b+1/3c, c; 0, 0, 0$), consistent with Ref. [30] as tabulated in MAGNDATA [39,40]. Assessment with onsite Coulombic interaction of d orbitals of Cr atoms is carried out with the simplified rotational invariant DFT + U approach introduced by Dudarev *et al.* [33]. The dependence of lattice parameter and total energy for different U_{eff} values are given in Table S1 within the SM [38]. For all $U_{\text{eff}} > 2$ eV values, FM spin order appears to be the ground state. For $U_{\text{eff}} = 1$ eV, the possible orderings with respective results of lattice parameters, moments, and total energy difference are given in Table I. The lattice parameter and magnetic moments per Cr atom comparison between experimental and computational results agree the most with FCFiM order. This confirms FCFiM is the ground state of rhombohedral Cr₂S₃, while the weak magnetization can stem from the probable reasons as noted in the previous paragraph. A slight energy variation in FiM-I and a comparably larger c lattice show a probable phase change upon deformation. On the other hand, the remarkable energy difference between FCFiM and NM states shows a strong magnetic interaction between Cr sites [41]. The Cr-S bond length of the ground state structure shows a slight variation between different octahedra for different Cr sites showing site-dependent crystal field variation.

Considering the different octahedral structures surrounding Cr atoms, site Cr(I) is observed to have a slightly shorter Cr-S bond length and wider S-Cr-S angle between octahedral ligands (Table II). The octahedral structure distortion in Cr(I) gives two different angles and bond lengths depending on the relative location of Cr(III). Detailed variations are observed based on the noncentral symmetric crystal structure of Cr₂S₃ generated by the alternating layers of Cr deficient/rich layers. Owing to the noncentral symmetric environment around different Cr sites, octahedrons made by surrounding ligands at Cr(I) site are asymmetric while symmetric in both Cr(II) and Cr(III) sites (Fig. S2). This onsite crystal field variation could support the anticipated temperature dependency of Cr magnetic moments as proposed in the previous report [30]. The shortest distance between two Cr atoms is found between every successive layer along the c axis. As will be discussed,

TABLE II. Cr₂S₃ ground state crystal structure site-dependent octahedral parameters: Cr-S bond length l_a ($S = S_{1,2,3}$) and l_b ($S = S_{4,5,6}$) (Å), and S-Cr-S bond angle θ_a ($S = S_{1,2,3}$) and θ_b ($S = S_{4,5,6}$). All measurements are referred to as octahedral in Fig. 1(c). (Detailed representation of each Cr-site octahedral can be referred to Fig S2 within the SM [38].)

Cr-Sites	l_a	l_b	θ_a	θ_b
Cr(I)	2.39	2.41	87.6	95.3
Cr(II)	2.41	2.41	88.3	88.3
Cr(III)	2.41	2.41	87.2	87.2

this short distance between site Cr(I) and Cr(III) seems to drive interlayer AFM coupling as confirmed by a stronger exchange coupling constant.

Having identified the magnetic ground state of Cr₂S₃, the detailed electronic properties are explained below. A spin-polarized calculation on band structures and total density of states in Figs. 2(a) and 2(b) unveils the potential BMS characteristics of the material. The spin-dependent band gap difference is observed. The band gap value for spin-up and spin-down is 0.5 and 1.01 eV, respectively, consistent with the experimental room temperature semiconducting property [26,27]. The global band gap ($\Delta 1$) is 0.45 eV, estimated from Fig. 2(a). Also, the spin-flip gap in the valence band ($\Delta 2$) is 0.05 eV, and the spin-flip gap in the conduction band ($\Delta 3$) is 0.56 eV. Note that the $\Delta 2$ energy gap is relatively small but about double thermal energy at room temperature. However, the $\Delta 3$ energy gap is large enough compared with thermal energy. Thus, one can expect fully spin-polarized current even at room temperature by applying a positive gate voltage, i.e., pushing up the Fermi level into $\Delta 3$, the spin-flip gap in the conduction band. In this regard, our calculation supports that Cr₂S₃ is fundamentally a bipolar magnetic semiconductor.

For realizing the BMS device, a small spin-flip gap $\Delta 2$ should be large enough to prevent the mixing of spin currents by thermal agitation. Also, a relatively small $\Delta 1$ would be better to shift the Fermi level into the CBM spin channel by moderate gating. Despite these limitations in its native form, Cr₂S₃ would have a role of a novel class of BMS material, for which mostly either functionalized material or Heusler-type were previously reported [43]. Not only the BMS but FCFiM feature could be valuable for so-called ferrimagnetic spintronics application, where weak or zero magnetic ferrimagnetic material is utilized for its advantage of robustness against crosstalk [44].

This BMS behavior is invariant for various U_{eff} values, as shown in Fig. S3 within SM [38]. Including spin-orbital coupling in the calculation does not significantly affect band dispersion, as shown in the Fig. S4 within SM [38]. Element-projected partial density of states (PDOS) in Fig. 2(b) shows the VBM in the spin-up channel is provided both d and p orbitals. In contrast, CBM is supplied with mainly d orbitals of Cr atoms. All p orbitals p_x , p_y , and p_z of S atoms have almost equal contributions to VBM, as shown in Fig. 2(c). Concerning this, one can see the three VBM valleys at the γ point for both spin channels belonging to p orbitals of the S atoms, as shown in Fig. S5 within the SM [38].

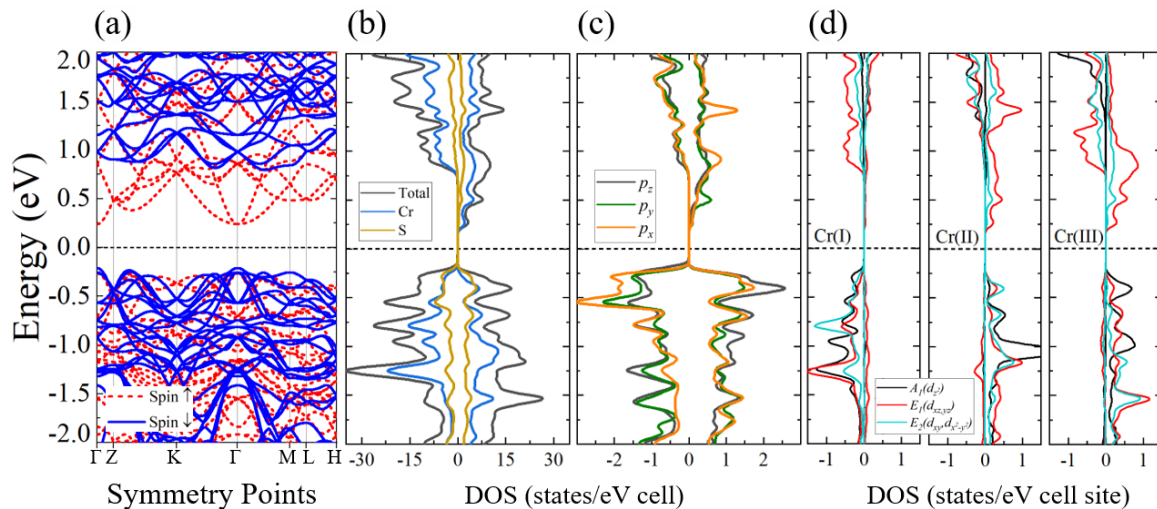


FIG. 2. (a) Electronic band structure of Cr_2S_3 with spin-up (red dashed line) and spin-down (blue solid line). (b) The total and element-projected partial density of states. (c) p -orbital projected PDOS for S and (d) Cr-site projected PDOS. The Fermi level is set to be zero, marked as a horizontal dashed line.

According to the ligand field theory, the Cr $3d$ -orbital states split into threefold degenerate t_{2g} (d_{xz} , d_{yz} , d_{xy}) and twofold degenerate e_g (d_{z^2} , $d_{x^2-y^2}$) orbital substates in a perfect octahedral crystal field. The structural distortion of CrS_6 octahedron (CdI₂-type structure) makes the e_g state further split into the $A_1(d_{z^2})$ and doubly degenerate $E_2(d_{x^2-y^2})$ states, while the t_{2g} state is divided into $E_1(d_{xz}, d_{yz})$ and $E_2(d_{xy})$ [45,46]. Therefore, the ab -plane crystal-field sets all in-plane states degenerate as $E_2(d_{xy}, d_{x^2-y^2})$. A schematic representation of distorted CrS_6 octahedron is shown in Fig. 1(c). Cr-site-dependent PDOS is demonstrated in Fig. 2(d). Each Cr site has a different d -states distribution near the Fermi level showing the crystal anisotropy and onsite crystal field variation. [E.g., Cr(III) has E1 and E2 DOS peaks at lower energy levels than A1, while Cr(I) has E2 at higher energy than E1 and A1]. This crystal field anisotropy becomes a fascinatingly useful knob to control the band structure and magnetic properties by straining the c axis, as will be discussed below. As clearly shown in the PDOS plot in Fig. 2(d), the half semiconducting behavior is caused by the Cr-site-dependent bandgap that stems from the combined effect of magnetic interaction, the difference in crystal field, and onsite exchange splitting energy [47]. Interestingly enough, the half-semiconducting behavior of Cr_2S_3 exists even in FM ordering (Figs. S4d and 4e), showing that it is embedded within the material's unique crystal structure. Regardless of the spin order, rhombohedral Cr_2S_3 shows a clear spin-polarized semiconducting gap.

Compensated states of the crystal structure are governed by both interlayer and intralayer AFM couplings of Cr atomic sites. Magnetic moments in each Cr atom are shown in Table I, which agree with Cr $3/2$ spin. The direct and superexchange interactions of Cr atoms at different sites can be explained by the Goodenough-Kanamori-Anderson (GKA) rules [48]. A robust direct AFM coupling between Cr(I) and Cr(III) is facilitated by a relatively short distance of 2.91 Å along with the c axis [46]. The distance between Cr(II) and Cr(III) is as considerable as 4.38 Å; therefore, the direct exchange between these two atoms becomes rather unlikely. The GKA rule

predicts if the cation-anion-cation bond angles are of 90° or 180° , two cation spins often favor weak FM and strong AFM ordering, respectively. For an angle of 134° between Cr(II) and Cr(III) [θ_2 in Fig. 5(d)], the competition between these two will result in distance-dependent interaction as Rukang Li *et al.* have proposed angle/distance-dependent interaction between octahedral-edge shared Mn-Mn interactions [49]. A similar examination between Cr(I) and Cr(II) shows that the competition between AFM via direct exchange and FM via superexchange results in AFM spin ordering as the ground state. For each Cr-rich layer, Cr(I) sites have neighboring Cr(II) sites within the layer. The trigonal positions of spins [Fig. 1(b)] might give rise to the frustrating spin order by competing between FM and AFM intralayer interactions. This might be responsible for the noncollinear spin order observed experimentally in the crystal structure [50].

We employ an effective Heisenberg model of classical spins to describe the interaction between Cr atoms. A schematic view of the nearest-neighbor exchange interaction between Cr atomic sites is shown in Fig. 3(a). Exchange coupling constants J_{ij} between site i and j are obtained by mapping the calculated total energy to the effective Heisenberg Hamiltonian, $H_{\text{eff}} = -\sum J_{ij} \mathbf{s}_i \cdot \mathbf{s}_j$, where \mathbf{s}_i is the unit vector parallel to spin \mathbf{s}_i , and J_{ij} is an exchange coupling constant for the nearest neighboring Cr atom for each site. In-plane and out-of-plane exchange interactions are shown in Fig. S6. We employed spin-flip energy differences for Cr atoms on each site to get energy differences. Out-of-plane AFM exchange coupling constant between Cr(I) and Cr(III) is calculated as $J_1 = -6.47$ meV, the most substantial interlayer interaction of the other nearest-neighbor exchange interactions. It plays a significant role in the magnetoelastic property of the material. Out-of-plane exchange coupling constant between Cr(II) and Cr(III) (J_2) is evaluated as 1.09 meV, exhibiting weak FM, while the planar exchange coupling constant between Cr(I) and Cr(II) (J_3) is calculated as -3.45 meV exhibiting AFM. With these J values, we applied molecular field theory to estimate the temperature dependence of

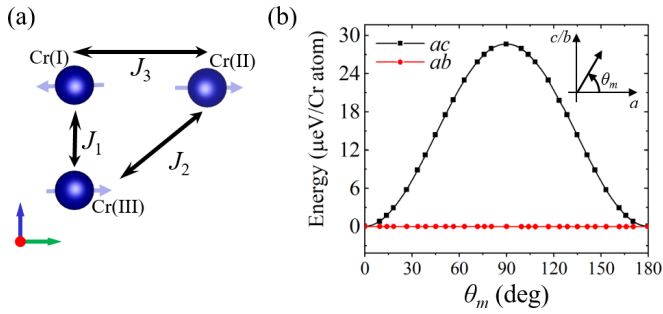


FIG. 3. (a) Schematic representation of exchange interactions between Cr atoms. The relative positions of atoms are paralleled with the axes of the crystal structure shown. Horizontal blue arrows represent spin order for each Cr site. (b) MAE as a function of magnetization angle θ_m for both in-plane (ab) and out-of-plane (ac). A geometry for out-of-plane magnetization angle θ_m and lattice a and c are shown (inset).

magnetization (M - T) [51]. The M - T curve within the SM [38] is evident in the characteristic feature of fully compensated ferrimagnetic materials, including the Heusler compound [52,53]. This clearly shows that the interplay between the three sublattice magnetization achieves full compensation. Moreover, the curve is qualitatively in good agreement with the experimental result of Yuzuri *et al.* for Cr₂S₃ [54].

Figure 3(b) shows the MAE calculated as a function of magnetization angle θ_m in both ab and ac planes. No substantial difference in energy upon rotation for different in-plane directions is observed from DFT calculations. In contrast, out-of-plane rotation shows an easy plane perpendicular to the c axis. Based on the hexagonal symmetry of crystal structure in the ab plane and localized magnetic moments, the angular dependence of the MAE on the magnetization angle θ_m in the ac or bc plane can be fit by the following equation, $\text{MAE}(\theta) = K_1 \sin^2(\theta) + K_2 \sin^4(\theta)$, where K_1 and K_2 are the magnetocrystalline anisotropy coefficients, and θ is measured

relative to the easy axis [55–57]. K_1 and K_2 are obtained as 28.67 and $-0.02 \mu\text{eV}/\text{Cr}$ by fitting, respectively. The calculated result on MAE of 0.336 meV per unit cell ($28 \mu\text{eV}/\text{Cr}$) shows that the easy axis lies in the ab plane (i.e., easy plane), which conforms to the experimental results [25,35,58]. A comparable value of MAE is also shown in a monolayer CrCl₃ [59].

As discussed above, the crystal structure has planar versus c -axis anisotropy in electronic and magnetic environments. Additionally, the interlayer interaction along the c axis is found to govern the crystal structure's magnetic ground state. Thus, we take the c -axis straining as a way to unveil and understand its unique BMS-FCFiM properties. Figure 4(a) shows the c -axis strain-induced energy variation of different magnetic phases. Here, the strain is defined as $\varepsilon = (c - c_0)/c_0$, where c_0 is the lattice constant for the relaxed system. Bilateral shrinkage plotting in Fig. 4(b) shows the bulk response of the ab plane upon the c -axis strain. In Fig. 4(a), the FCFiM property of the crystal is well-preserved up to a considerable uniaxial c -axis compression strain value up to -6% (the equivalent of a biaxial tensile strain of $+1.6\%$) as shown in Fig. 4(a).

In comparison, a tensile strain of $+2\%$ (the equivalent of a biaxial compressive strain of -0.4%) induces a magnetic phase transition to ferrimagnetic order FiM-I. Above this tensile strain value, interlayer FM superexchange interaction through cation becomes more appealing energetically than the AFM direct hopping of d -orbital electrons from Cr(I) to Cr(III). Moreover, interlayer magnetic coupling is FM, while the intralayer coupling is maintained as AFM.

A closer look at the respective distance of Cr atoms at sites I and III (d_1) unveils that the substantial orbital overlap (thereby AFM interaction) fades as a positive strain is applied along the c axis [60]. Consequently, the ground state spin order is changed from FCFiM to ferrimagnetic (FiM-I). This phenomenon is accompanied by an abrupt Cr atom positioning on sites I and III, as shown in Fig. 5(a). The nearest Cr-Cr

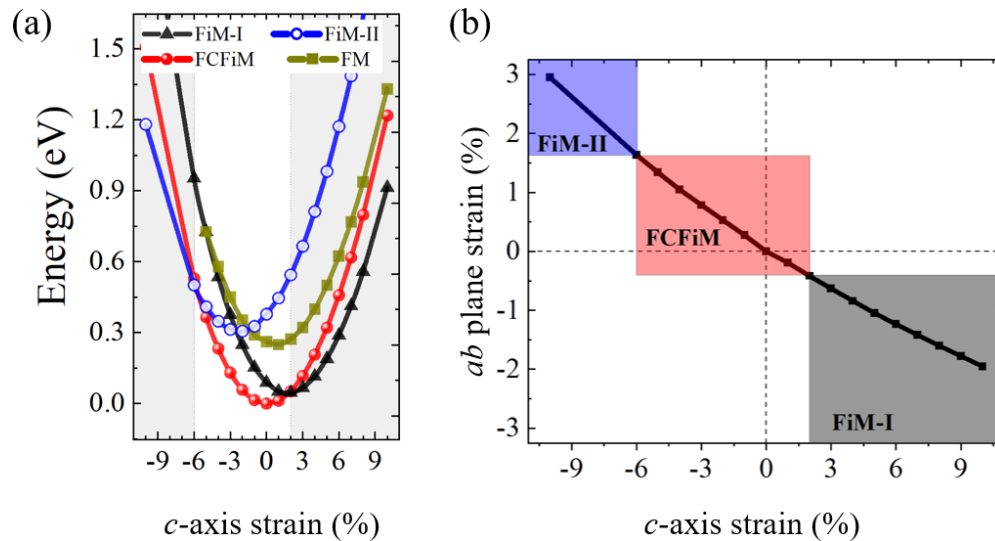


FIG. 4. The magnetic ground state of Cr₂S₃ under the c -axis uniaxial strain. (a) Relative total energies of four different collinear magnetic configurations (FM, FCFiM, FiM-I, and FiM-II, shown in Fig. S1) as a function of uniaxial strain along the c axis. (b) Bulk elastic response (equivalent ab -plane strain) upon the c -axis strain. The color for the parabola in (a) and shadings in (b) are meant to match.

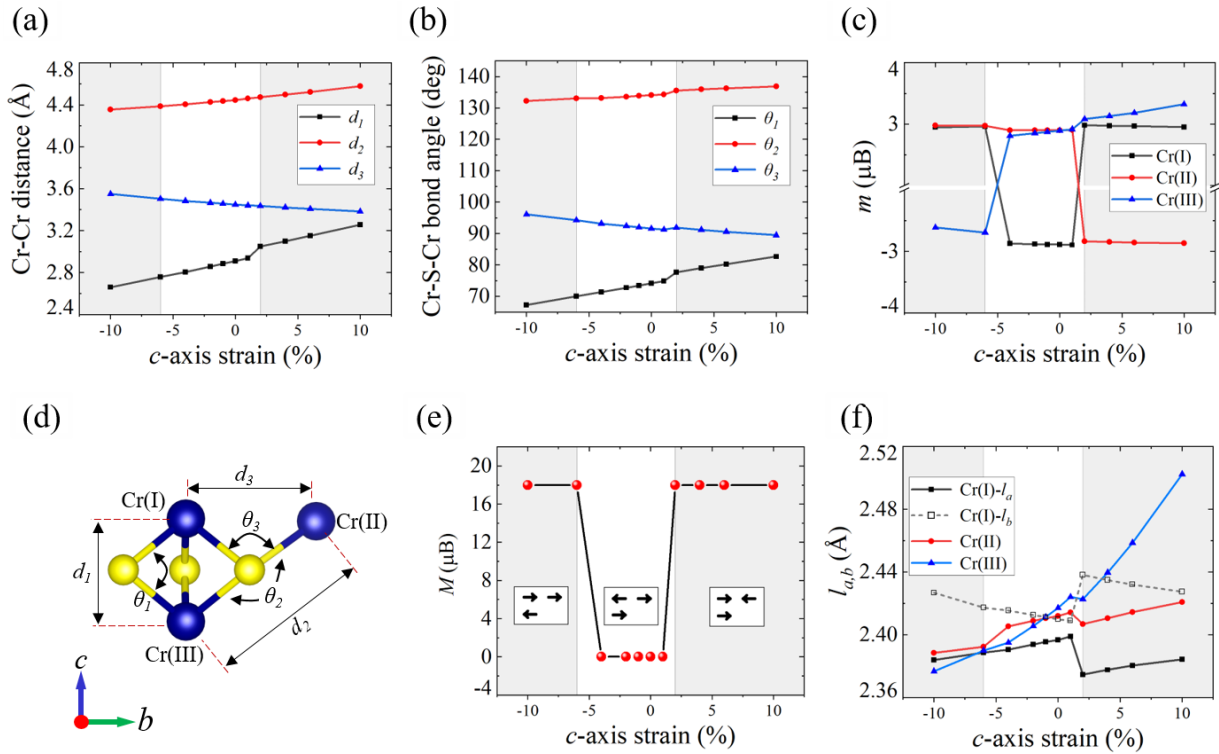


FIG. 5. Dependence of structural parameters and magnetic moment on c -axis strain (ε) for Cr_2S_3 . (a) Cr–Cr distances. (b) Cr–S–Cr bond angles (c) Magnetic moment m for different sites of Cr atom. (d) Schematic representation of the relative position of Cr sites. (e) The total magnetic moment M per unit cell. Spin orientation for each phase is shown in the inset following relative position shown in (c). (f) Cr–S bond lengths (l_a and l_b) in CrS_6 octahedral for all three Cr sites. Note that l_a and l_b for Cr(I) are different and are plotted with black solid and dashed lines, respectively. Vertically shaded regions are drawn as a guide to the eye, indicating different magnetic phases.

atom distances d_1 and d_2 go linear with the c -axis strain, while d_3 exhibits an abrupt change at the phase transition strain. This indicates a strong underlying magnetoelastic coupling in “sublayers” of Cr_2S_3 . This phenomenon goes in line with the recent high-throughput prediction of Luis Casillas *et al.*, demonstrating a strong magnetostructural coupling in Cr_2S_3 [61]. Furthermore, Raman active redshifts of the interlayer breathing mode reported in Yang *et al.* confirm the strain-sensitive interlayer interaction in Cr_2S_3 [29].

Strain-dependent Cr–S–Cr angle variations shown in Fig. 5(b) similarly indicates an abrupt change at the critical strain. Further increment in strain will only show monotonically increasing Cr–Cr distances and thus stabilize the FiM-I phase. It is worth noting that the abrupt change in Cr–S–Cr angle gets more pronounced in θ_1 than in θ_2 and θ_3 .

The crystal anisotropy (ab plane versus c axis) and two different Cr–S bond lengths together with magnetic interaction have led to the material’s BMS fully compensated property. It should be noted that the l_a of Cr(I) is experiencing a slight change upon compression. The slopes differences in Figs. 5(a) and 5(b) are attributed to the Poisson’s ratio, $\nu = 0.19$. The strain-induced phase transition from FCFiM to FiM-I causes an abrupt VBM and CBM for spin-down only, as shown in Fig. S7a.

Magnetic moments at Cr sites are plotted against strain in Fig. 5(c). Cr(II) and Cr(III) sites show spin-flip at the critical strain values for FiM-II and FiM-I, respectively. Moreover, due to the charge transfer effect, the sulfur atom has a total

moment of 0.07 and 0.063 μB upon phase transition from FCFiM to FiM-I and FiM-II, respectively [62]. In Fig. 5(e), considerable change is shown in the total magnetic moment per unit cell at both magnetic phase changes, making Cr_2S_3 a promising candidate for piezomagnetism.

Figure 5(f) shows the change in bond lengths of three Cr-centered octahedral structures upon c -axis straining. As pointed out in Table II and Fig. S2, Cr(I) has a slightly shorter bond length with S ligands in the direction where Cr(III) is not facing Cr(I) directly along the c axis. The symmetrical octahedral structure around Cr(II) and Cr(III) shows that the uniaxial tensile/compression strain along the c axis makes the bonds longer/shorter except at phase transition points. However, for the case of Cr(I), l_a increases while the l_b decreases upon tensile straining. Moreover, at the strain of +2%, both show a more pronounced change in bond length opposite to the trend in the tensile strain region. This phenomenon is matched with the sudden change in Cr–Cr distance in Fig. 5(a), which explains the enhanced difference in bond length.

To qualitatively illustrate the changes in the electronic properties of Cr_2S_3 with uniaxial c -axis strain, we have produced spin-polarized band structure, the p -orbital PDOS, and site-projected DOS for three Cr sites as shown in Fig. 6. As shown in Figs. 6(a)–6(e), a direct bandgap (at Γ point) property is well preserved under both compression and tensile strain range except the compression limit of -6% in which the material is changed to be an indirect (Γ -M) semiconductor with a finite net magnetic moment (FiM-II). Upon

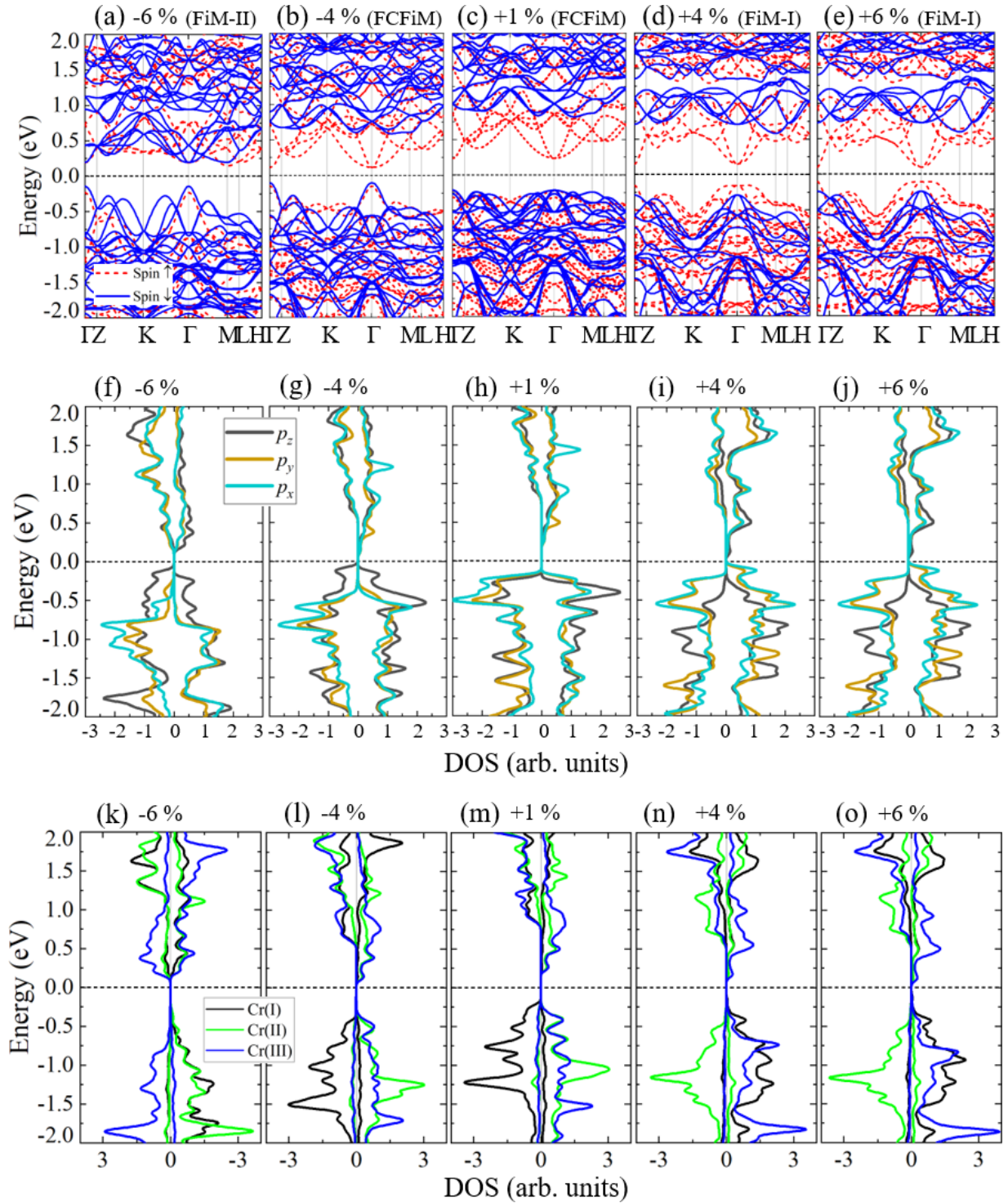


FIG. 6. The dependence of electronic band structure and projected DOS of Cr₂S₃ on the various *c*-axis strain. (a)–(e) Band structures for compressive and tensile strains of (a) -6% , (b) -4% , (c) $+1\%$, (d) $+4\%$, and (e) $+6\%$ with spin-up/down (red-dashed/blue-solid). (f)–(j) S-3p PDOS, (k)–(o) Cr-3d site-projected PDOS under different corresponding strains to (a)–(e). The zero of energy is at the Fermi level, marked as a horizontal dashed line. The magnetic ground state is indicated with FCFiM, FiM-I, and FiM-II.

further compression strain (-10%), Cr₂S₃ becomes metallic (Fig. S7). Intending to see the underlying principle behind this loss of BMS property at -6% strain, we carefully traced the crystal structure deformation pattern by observing the octahedron bond length change for each site upon straining, which will be discussed below.

The VBM and CBM of the band structure tend to show a slight variation even with higher strain values, indicating a localized *d* states characteristic. Interestingly enough, however, an abrupt change in VBM and CBM is observed at the magnetic transition strains for FiM-II and FiM-I phases, respectively [Figs. 6(a) and 6(e)]. FiM-I and FiM-II are

coupled with interlayer and intralayer magnetic phase transition, respectively. This can clearly indicate different d - d hybridization schemes near the Fermi level. We did a non-magnetic calculation to elucidate this observation and checked each site's contribution below and above Fermi level (Fig. S4a). The result indicates that the states near the Fermi level (within ± 0.2 eV) have more contribution of $d_{x^2-y^2}$, d_{xy} , and d_{z^2} from Cr(I) and Cr(II). In comparison, states distant from the Fermi level (± 1.0 eV) have more contribution of d_{xz} , d_{yz} , and d_{z^2} from Cr(I) and Cr(III) d orbitals indicating different d - d hybridization in the in-plane and out-of-plane crystal direction [63]. This result is in line with the fact that the connectivity of octahedral structures in a crystal structure determines the d - d hybridizations between central metal atoms [64]. Here an edge-shared octahedral structure is formed between Cr(I) and Cr(II), while a face-shared octahedral structure is formed between Cr(I) and Cr(III).

As discussed above, because of the magnetoelastic property of the Cr_2S_3 , the transition in magnetic coupling between Cr(I) and Cr(III) atoms from FCFiM to FiM will further facilitate Cr atoms to move apart. As a result, a strongly distorted octahedral structure in Cr(I) and Cr(III) and bond lengths are presented. Furthermore, this pronounced distortion combined with the magnetic phase transition has resulted in a spin-polarized VBM, as shown in Figs. 6(d) and 6(e). Cr(I) shares the same S atoms with Cr(III) directly on the top with a relatively long bond length l_b . A compressive strain along the c axis causes all l_b to decrease monotonically except for Cr(I), which shows a slight increase [Fig. 5(f)].

At the compressive strain value of -6% , relatively equal l_b are formed in all Cr sites except for Cr(I). This could give rise to the indifference of Cr sites since the crystal field generated by the six S atoms surrounding each Cr atom would be the same due to relatively equal bond lengths. Here we assume that l_b at Cr(I) will have an insignificant effect since the shorter l_a will elevate the energy of d states. Considering the magnetic in-plane interaction between Cr(I) and Cr(II), the direct AFM interaction is weakened as the in-plane tensile strain is associated with the compressed c -axis lattice. Instead, superexchange interaction via S atoms gets strengthened and starts to dominate at the critical strain of -6% .

The interlayer magnetic coupling between Cr(I) and Cr(III) is AFM under any compression strain. Therefore, at that point, the in-plane FM and out-of-plane AFM interactions are set. Because all Cr atoms feel almost the same octahedral ligand crystal field (due to nearly the same Cr-S bond lengths), Cr_2S_3 would have spin-degenerate states for spin-up and spin-down channels. That means Cr_2S_3 is changed to a ferrimagnetic material with a trivial semiconducting property, i.e., the BMS property is lost. This result then helps us to see the rationale behind the extraordinary BMS FCFiM property of Cr_2S_3 .

The HS characteristic can be revealed under the tensile strain larger than $+1\%$, where VBM in each spin channel is leveled. For example, at $+4\%$, the VBM and CBM are located in the same spin channel, while the other spin channel maintains a relatively large gap. In practice, the 4% uniaxial tensile straining is hard to achieve; however, the equivalent biaxial compression within the basal plane is -0.8% , which would be more accessible. The spin degeneracy of VBM is removed for the tensile strains $\geq +2\%$, which reflects a

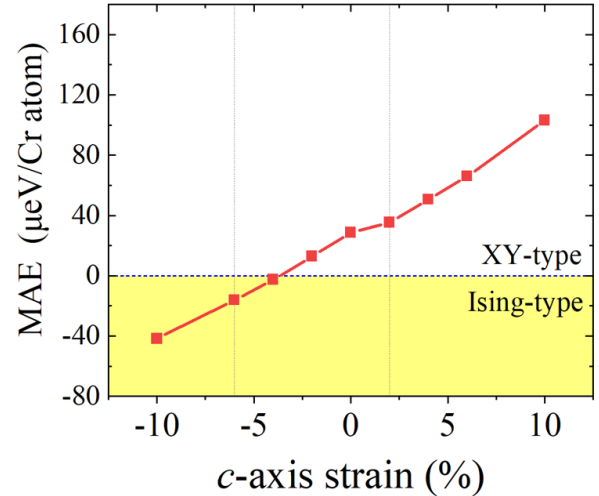


FIG. 7. The variation of MAE value of Cr_2S_3 under uniaxial c -axis strain. Vertical lines at each strain range separate the corresponding magnetic ground states (FiM-II, FCFiM, FiM-I). The horizontal shaded region splits XY- and Ising-type spin orderings.

decrease of electron hopping and reduced AFM coupling strength between Cr(I) and Cr(III) due to strong confinement of orbitals by tensile strain [60]. Figures 6(f)–6(j) shows the PDOS of the p orbitals of S. In-plane p_x and p_y orbitals behave opposite to the out-of-plane p_z orbitals, associated with positive Poisson's ratio. Upon compressive strain, S - p_x and S - p_y PDOS near VBM move away from the Fermi level while S - p_z PDOS moves towards the Fermi level in both spin channels.

This again evidences the crystal anisotropy selectively controlling VBM and CBM by tensile and compressive strains, respectively. S - p PDOS at zero strain shows degenerate spin states of VBM at Γ with FCFiM magnetic order [Fig. 2(c)]. However, after the material becomes ferrimagnetic (FiM-I), these S - p PDOS show spin polarization where spin-up states are at higher energy than spin-down states near the Fermi level, as shown in PDOS in Figs. 6(i) and 6(j).

To determine the different Cr site contributions at each strain, we plotted the site-dependent Cr- d PDOS in Figs. 6(k)–6(o). In the FCFiM magnetic phase (at -4% and $+1\%$ strain), all Cr sites contribute to the VBM (therefore degenerate spin-up and spin-down states). In contrast, ferromagnetically interacting Cr(II) and Cr(III) only contribute to the CBM. Thus, spin-polarized CBM appears. In the FiM-I phase (at $+4\%$ and $+6\%$), the spin-polarized CBM is maintained. At the same time, the VBM becomes spin-polarized in the states near the Fermi level, coming from ferromagnetically interacting spin-up states of Cr(I) and Cr(III). This trend continues and eventually makes Cr_2S_3 half-metallic at $+10\%$ strain (Fig. S7a).

MAE dependence on uniaxial c -axis straining indicates monotonically increasing/decreasing MAE upon tensile/compressive strain, as shown in Fig. 7. A tensile strain would continue to enforce the ab plane as an easy plane keeping the Cr_2S_3 XY-type, where spins are confined within the 2D easy plane. Around the compressive strain of -4% , a transition from easy-plane to easy-axis (c axis) starts, leading

to Cr₂S₃ Ising-type. A similar shift from easy-plane to easy-axis magnetic anisotropy was shown in the CrCl₃ monolayer upon biaxial strain [59]. As discussed above, further compression would only increase the MAE and change the magnetic phase to FiM-II. A tensile strain of 5% would double MAE to 56 meV. The slight slope change is associated with phase transition into FiM-I, where interlayer interaction changed from AFM to FM. On the other hand, the slope does not change by the transition from FCFiM to FiM-II, where planar spin-flip occurs.

IV. CONCLUSIONS

We have applied DFT calculations to investigate the magnetic and electronic properties of Cr₂S₃. The magnetic ground state is FCFiM in accordance with the previous experimental findings. The origin of BMS/HS and the FCFiM state has been explained by a structural analysis, where magnetic exchange interaction between Cr sites is dependent on bond distance and

bond angle of each Cr-centered octahedron. Furthermore, by applying strains perpendicular to the basal plane, distortion of Cr octahedron sites and Cr–Cr distance is controlled, resulting in the phase transition of the material both electronically and magnetically from BMS-FCFiM to FiM-semiconductor. The unique BMS-FCFiM and magnetoelastic property suggest Cr₂S₃ as a promising material for next-generation spintronic applications.

ACKNOWLEDGMENTS

This work has been supported by the National Research Foundation of Korea (Grants No. NRF-2016R1A6A3A11934734 and No. NRF-2019R1I1A1A01061466). The computational resource has been provided by the Korea Institute of Science and Technology Information (KISTI) (KSC-2014-C2-041, KSC-2020-CRE-0325). A research grant from Sungkyunkwan University supported this work.

-
- [1] H. Van Leuken and R. A. de Groot, Half-Metallic Antiferromagnets, *Phys. Rev. Lett.* **74**, 1171 (1995).
- [2] X. L. Wang, Proposal for a New Class of Materials: Spin Gapless Semiconductors, *Phys. Rev. Lett.* **100**, 156404 (2008).
- [3] X. Hu, Half-metallic antiferromagnet as a prospective material for spintronics, *Adv. Mater.* **24**, 294 (2012).
- [4] S. A. Wolf, D. D. Awschalom, R. A. Buhrman, J. M. Daughton, S. Von Molnár, M. L. Roukes, A. Y. Chtchelkanova, and D. M. Treger, Spintronics: A spin-based electronics vision for the future, *Science* **294**, 1488 (2001).
- [5] R. A. de Groot, Half-metallic magnetism in the 1990s, *Phys. B* **172**, 45 (1991).
- [6] W. E. Pickett, Spin-density-functional-based search for half-metallic antiferromagnets, *Phys. Rev. B* **57**, 10613 (1998).
- [7] W. E. Pickett and J. S. Moodera, Half metallic magnets, *Phys. Today* **54**, 39 (2001).
- [8] H. Akai and M. Ogura, Half-Metallic Diluted Antiferromagnetic Semiconductors, *Phys. Rev. Lett.* **97**, 026401 (2006).
- [9] J. He, P. Zhou, N. Jiao, X. Chen, W. Lu, and L. Z. Sun, Prediction of half-semiconductor antiferromagnets with vanishing net magnetization, *RSC Adv.* **5**, 46640 (2015).
- [10] F. Cervantes-Sodi, G. Csányi, S. Piskanec, and A. C. Ferrari, Edge-functionalized and substitutionally doped graphene nanoribbons: Electronic and spin properties, *Phys. Rev. B* **77**, 165427 (2008).
- [11] J. Kübler, A. R. William, and C. B. Sommers, Formation and coupling of magnetic moments in heusler alloys, *Phys. Rev. B* **28**, 1745 (1983).
- [12] R. A. de Groot, F. M. Mueller, P. G. van Engen, and K. H. J. Buschow, New Class of Materials: Half-Metallic Ferromagnets, *Phys. Rev. Lett.* **50**, 2024 (1983).
- [13] S. Ouardi, G. H. Fecher, C. Felser, and J. Kübler, Realization of Spin Gapless Semiconductors: The Heusler Compound Mn₂CoAl, *Phys. Rev. Lett.* **110**, 1004012 (2013).
- [14] H. Kurt, K. Rode, P. Stamenov, M. Venkatesan, Y. C. Lau, E. Fonda, and J. M. D. Coey, Cubic Mn₂Ga Thin Films: Crossing the Spin Gap with Ruthenium, *Phys. Rev. Lett.* **112**, 027201 (2014).
- [15] S. Semboshi, R. Y. Umetsu, Y. Kawahito, and H. Akai, New type of half-metallic fully compensated ferrimagnet, doi: [10.21203/rs.3.rs-1572952/v1](https://doi.org/10.21203/rs.3.rs-1572952/v1).
- [16] C. Gong, L. Li, Z. Li, H. Ji, A. Stern, Y. Xia, T. Cao, W. Bao, C. Wang, Y. Wang, Z. Q. Qiu, R. J. Cava, S. G. Louie, J. Xia, and X. Zhang, Discovery of intrinsic ferromagnetism in two-dimensional van der waals crystals, *Nature (London)* **546**, 265 (2017).
- [17] B. Huang, G. Clark, E. Navarro-Moratalla, D. R. Klein, R. Cheng, K. L. Seyler, Di. Zhong, E. Schmidgall, M. A. McGuire, D. H. Cobden, W. Yao, D. Xiao, P. Jarillo-Herrero, and X. Xu, Layer-dependent ferromagnetism in a van der waals crystal down to the monolayer limit, *Nature (London)* **546**, 270 (2017).
- [18] Y. Guo, B. Wang, X. Zhang, S. Yuan, L. Ma, and J. Wang, Magnetic two-dimensional layered crystals meet with ferromagnetic semiconductors, *InfoMat* **2**, 639 (2020).
- [19] M. C. Wang, C. C. Huang, C. H. Cheung, C. Y. Chen, S. G. Tan, T. W. Huang, Y. Zhao, Y. Zhao, G. Wu, Y. P. Feng, H. C. Wu, and C. R. Chang, Prospects and opportunities of 2D van Der Waals magnetic systems, *Ann. Phys.* **532**, 1900452 (2020).
- [20] X. Li, X. Wu, Z. Li, J. Yang, and J. G. Hou, Bipolar magnetic semiconductors: A new class of spintronics materials, *Nanoscale* **4**, 5680 (2012).
- [21] J. Zhang, X. Li, and J. Yang, SiN-SiC nanofilm: A nano-functional ceramic with bipolar magnetic semiconducting character, *Appl. Phys. Lett.* **104**, 172403 (2014).
- [22] J. He, P. Lyu, L. Z. Sun, Á. Morales García, and P. Nachtigall, High temperature spin-polarized semiconductivity with zero magnetization in two-dimensional janus mxenes, *J. Mater. Chem. C* **4**, 6500 (2016).
- [23] J. Zhang, X. Li, and J. Yang, Electrical control of carriers' spin orientation in the fevtisi heusler alloy, *J. Mater. Chem. C* **3**, 2563 (2015).
- [24] A. Maignan, E. Guilmeau, F. Gascoin, Y. Bréard, and V. Hardy, Revisiting some chalcogenides for thermoelectricity, *Sci. Technol. Adv. Mater.* **13**, 053003 (2012).
- [25] J. Chu, Y. Zhang, Y. Wen, R. Qiao, C. Wu, P. He, L. Yin, R. Cheng, F. Wang, Z. Wang, J. Xiong, Y. Li, and J. He,

- Sub-millimeter-scale growth of one-unit-cell-thick ferrimagnetic Cr_2S_3 nanosheets, *Nano Lett.* **19**, 2154 (2019).
- [26] F. Cui, X. Zhao, J. Xu, B. Tang, Q. Shang, J. Shi, Y. Huan, J. Liao, Q. Chen, Y. Hou, Q. Zhang, S. J. Pennycook, and Y. Zhang, Controlled growth and thickness-dependent conduction-type transition of 2D ferrimagnetic Cr_2S_3 semiconductors, *Adv. Mater.* **32**, 1905896 (2020).
- [27] L. Xie, J. Wang, J. Li, C. Li, Y. Zhang, B. Zhu, Y. Guo, Z. Wang, and K. Zhang, An atomically thin air-stable narrow-gap semiconductor Cr_2S_3 for broadband photodetection with high responsivity, *Adv. Electron. Mater.* **7**, 2000962 (2020).
- [28] C. Li, F. Ke, Q. Hu, Z. Yu, J. Zhao, Z. Chen, and H. Yan, Correlated structural and electronic phase transformations in transition metal chalcogenide under high pressure, *J. Appl. Phys.* **119**, 135901 (2016).
- [29] W. Yang, A. L. Coughlin, L. Webster, G. Ye, K. Lopez, H. A. Fertig, R. He, J. A. Yan, S. Zhang, and S. Yoshida, Highly tunable raman scattering and transport in layered magnetic Cr_2S_3 nanoplates grown by sulfurization, *2D Mater.* **6**, 035029 (2019).
- [30] E. F. Bertaut, J. Cohen, B. Lambert-Andron, and P. Mollard, Étude de Cr_2S_3 rhomboédrique par diffraction neutronique et mesures magnétiques, *J. Phys. (Paris)* **29**, 813 (1968).
- [31] G. Kresse, Efficient iterative schemes for *ab initio* total-energy calculations using a plane-wave basis set, *Phys. Rev. B* **54**, 11169 (1996).
- [32] J. P. Perdew, K. Burke, and M. Ernzerhof, Generalized Gradient Approximation Made Simple, *Phys. Rev. Lett.* **77**, 3865 (1996).
- [33] S. Dudarev and G. Botton, Electron-energy-loss spectra and the structural stability of nickel oxide: An LSDA+U study, *Phys. Rev. B* **57**, 1505 (1998).
- [34] J. Hendrik, Monkhorst, and James D. Pack, Special points for brillouin zone integrations, *Phys. Rev. B* **13**, 5188 (1976).
- [35] T. J. A. Popma, C. Haas, and B. Van Laar, Spin structure and magnetic anisotropy of Cr_5S_6 and rhombohedral Cr_2S_3 , *J. Phys. Chem. Solids* **32**, 581 (1971).
- [36] M. Mikami, K. Igaki, and N. Ohashi, Electrical and magnetic properties of the chromium sulfide with deviation from stoichiometric composition Cr_2S_3 , *J. Phys. Soc. Jpn.* **32**, 1217 (1972).
- [37] Y. Motoyoshi and N. Yoji, Origin of ferrimagnetism in compounds Cr_5S_6 and Cr_2S_3 , *J. Phys. Soc. Jpn.* **19**, 1350 (1964).
- [38] See Supplemental Material at <http://link.aps.org/supplemental/10.1103/PhysRevMaterials.6.054405> for additional figures.
- [39] S. V. Gallego, J. M. Perez-Mato, L. Elcoro, E. S. Tasci, R. M. Hanson, K. Momma, M. I. Aroyo, and G. Madariaga, MAGNDATA: Towards a database of magnetic structures. I. the commensurate case, *J. Appl. Crystallogr.* **49**, 1750 (2016).
- [40] S. V. Gallego, J. M. Perez-Mato, L. Elcoro, E. S. Tasci, R. M. Hanson, M. I. Aroyo, and G. Madariaga, MAGNDATA: Towards a database of magnetic structures. II. the incommensurate case, *J. Appl. Crystallogr.* **49**, 1941 (2016).
- [41] Y. Jiao, F. Ma, C. Zhang, J. Bell, S. Sanvito, and A. Du, First-Principles Prediction of Spin-Polarized Multiple Dirac Rings in Manganese Fluoride, *Phys. Rev. Lett.* **119**, 016403 (2017).
- [42] A. Maignan, Y. Bréard, E. Guilmeau, and F. Gascoin, Transport, thermoelectric, and magnetic properties of a dense Cr_2S_3 Ceramic, *J. Appl. Phys.* **112**, 013716 (2012).
- [43] X. Li and J. Yang, First-principles design of spintronics materials, *Natl. Sci. Rev.* **3**, 365 (2016).
- [44] S. K. Kim, G. S. D. Beach, K. J. Lee, T. Ono, T. Rasing, and H. Yang, Ferrimagnetic spintronics, *Nat. Mater.* **21**, 24 (2022).
- [45] M. Chhowalla, H. S. Shin, G. Eda, L. J. Li, K. P. Loh, and H. Zhang, The chemistry of two-dimensional layered transition metal dichalcogenide nanosheets, *Nat. Chem.* **5**, 263 (2013).
- [46] J. Y. Chen, X. X. Li, W. Z. Zhou, J. L. Yang, F. P. Ouyang, and X. Xiong, Large-spin-gap nodal-line half-metal and high-temperature ferromagnetic semiconductor in Cr_2X_3 ($X = \text{O}, \text{S}, \text{Se}$) monolayers, *Adv. Electron. Mater.* **6**, 1900490 (2020).
- [47] C. Huang, J. Feng, F. Wu, D. Ahmed, B. Huang, H. Xiang, K. Deng, and E. Kan, Toward intrinsic room-temperature ferromagnetism in two-dimensional semiconductors, *J. Am. Chem. Soc.* **140**, 11519 (2018).
- [48] J. B. Goodenough, An interpretation of the magnetic properties of the perovskite-type mixed crystals $\text{La}_{1-x}\text{Sr}_x\text{CoO}_{3-\lambda}$, *J. Phys. Chem. Solids* **6**, 287 (1958).
- [49] R. Li, R. I. Smith, and C. Greaves, BiMnPO_5 with ferromagnetic $\text{Mn}^{2+}-(\mu-\text{O})_2-\text{Mn}^{2+}$ units: A model for magnetic exchange in edge-linked Mn^{2+}O_6 octahedra, *Chem. Commun.* **57**, 7027 (2021).
- [50] Y. Adachi, M. Yuzuri, M. Ohashi, T. Kaneko, Y. Yamaguchi, S. Funahashi, and Y. Morii, Magnetic structure of rhombohedral Cr_2Se_3 , *J. Phys. Soc. Jpn.* **63**, 1548 (1994).
- [51] S. ichi Ohkoshi, T. Iyoda, A. Fujishima, and K. Hashimoto, Magnetic properties of mixed ferro-ferrimagnets composed of prussian blue analogs, *Phys. Rev. B* **56**, 11642 (1997).
- [52] S. Wurmehl, H. C. Kandpal, G. H. Fecher, and C. Felser, Valence electron rules for prediction of half-metallic compensated- ferrimagnetic behaviour of heusler compounds with complete spin polarization, *J. Phys.: Condens. Matter* **18**, 6171 (2006).
- [53] R. Stinshoff, A. K. Nayak, G. H. Fecher, B. Balke, S. Ouardi, Y. Skourski, T. Nakamura, and C. Felser, Completely compensated ferrimagnetism and sublattice spin crossing in the half-metallic heusler compound $\text{Mn}_{1.5}\text{FeV}_{0.5}\text{Al}$, *Phys. Rev. B* **95**, 060410 (2017).
- [54] M. Yuzuri, T. Kaneko, T. Tsushima, S. Miura, S. Abe, G. Kido, and N. Nakagawa, Magnetic properties of Cr_2S_3 , *J. Phys. (Paris) Colloq.* **49**, C8-231 (1988).
- [55] R. C. O'Handley, *Modern Magnetic Materials: Principles and Applications* (Wiley, New York, 1999).
- [56] A. N. Bogdanov and I. E. Dragunov, Metastable states, spin-reorientation transitions, and domain structures, *Low Temp. Phys* **24**, 852 (1998).
- [57] H. L. Zhuang, P. R. C. Kent, and R. G. Hennig, Strong anisotropy and magnetostriction in the two-dimensional stoner ferromagnet Fe_3GeTe_2 , *Phys. Rev. B* **93**, 134407 (2016).
- [58] P. Vaqueiro, A. V. Powell, A. I. Coldea, C. A. Steer, I. M. Marshall, S. J. Blundell, J. Singleton, and T. Ohtani, Colossal magnetoresistance in the layered chromium sulfide $\text{Cr}_2\text{S}_{3-x}$ ($X = 0.08$), *Phys. Rev. B* **64**, 132402 (2001).
- [59] L. Webster and J. A. Yan, Strain-tunable magnetic anisotropy in monolayer CrCl_3 , CrBr_3 , and CrI_3 , *Phys. Rev. B* **98**, 144411 (2018).
- [60] Q. U. Ain, S. Naseem, and S. Nazir, Robust half-metallicity and magnetic phase transition in $\text{Sr}_2\text{CrReO}_6$ via strain engineering, *Sci. Rep.* **10**, 13778 (2020).
- [61] L. Casillas-Trujillo, R. Armiento, and B. Alling, Identification of materials with strong magnetostructural coupling using computational high-throughput screening, *Phys. Rev. Mater.* **5**, 034417 (2021).
- [62] J. Zaanen, and G. A. Sawatzky, Band Gaps and Electronic

- Structure of Transition-Metal Compounds, *Phys. Rev. Lett.* **55**, 418 (1985).
- [63] P. Pradia, R. Kashikar, A. Jena, and B. R. Kumar Nadra, Universality in the electronic structure of 3d transition metal oxides, *J. Phys. Chem. Solids* **123**, 133 (2018).
- [64] Z. Deng, G. Kieslich, P. D. Bristowe, A. K. Cheetham, and S. Sun, Octahedral connectivity and its role in determining the phase stabilities and electronic structures of low-dimensional, perovskite-related iodoplumbates, *APL Mater.* **6**, 114202 (2018).